

See discussions, stats, and author profiles for this publication at: <https://www.researchgate.net/publication/51039560>

Joint Experimental and Theoretical Analysis of Order Disorder Effects in Cubic BaZrO₃ Assembled Nanoparticles under Decaoctahedral Shape

ARTICLE in THE JOURNAL OF PHYSICAL CHEMISTRY A · MAY 2011

Impact Factor: 2.69 · DOI: 10.1021/jp1119124 · Source: PubMed

CITATIONS

18

READS

21

8 AUTHORS, INCLUDING:



Valéria Moraes Longo

Kairós Lab

59 PUBLICATIONS 1,195 CITATIONS

SEE PROFILE



J. R. Sambrano

São Paulo State University

90 PUBLICATIONS 1,415 CITATIONS

SEE PROFILE



Jose A. Varela

São Paulo State University

838 PUBLICATIONS 13,014 CITATIONS

SEE PROFILE



Elson Longo

São Paulo State University

876 PUBLICATIONS 14,988 CITATIONS

SEE PROFILE

Joint Experimental and Theoretical Analysis of Order–Disorder Effects in Cubic BaZrO₃ Assembled Nanoparticles under Decaoctahedral Shape

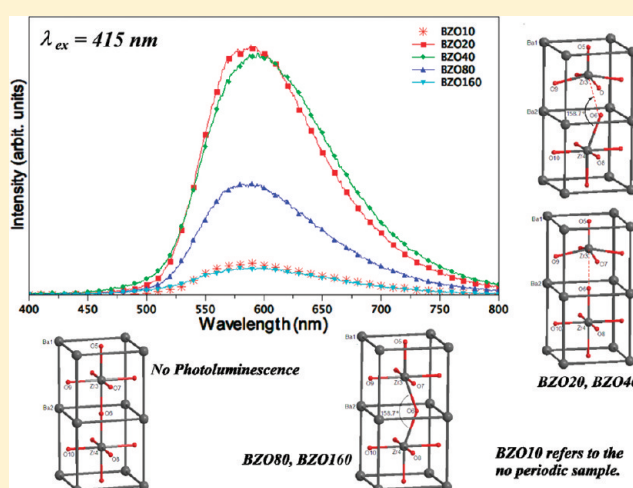
Mário Lúcio Moreira,^{*,†} Prescila Glaucia Cristianine Buzolin,[‡] Valeria Moraes Longo,[‡] Nelio Henrique Nicoleti,[‡] Julio Ricardo Sambrano,[‡] Maximu S. Li,[§] José Arana Varela,[‡] and Elson Longo[†]

[†]Instituto de Química, LIEC, INCTMN, Universidade Estadual Paulista, 14801-970, Araraquara, São Paulo, Brazil

[‡]Grupo de Modelagem e Simulação Molecular, DM, INCTMN, Universidade Estadual Paulista, P.O. Box 473, 17033-360 Bauru, Brazil

[§]Instituto de Física, Universidade de São Paulo, P.O. Box 369, 13560-970, São Carlos, São Paulo, Brazil

ABSTRACT: Periodic first-principles calculations based on density functional theory at the B3LYP level has been carried out to investigate the photoluminescence (PL) emission of BaZrO₃ assembled nanoparticles at room temperature. The defect created in the nanocrystals and their resultant electronic features lead to a diversification of electronic recombination within the BaZrO₃ band gap. Its optical phenomena are discussed in the light of photoluminescence emission at the green–yellow region around 570 nm. The theoretical model for displaced atoms and/or angular changes leads to the breaking of the local symmetry, which is based on the refined structure provided by Rietveld methodology. For each situation a band structure, charge mapping, and density of states were built and analyzed. X-ray diffraction (XRD) patterns, UV–vis measurements, and field emission scanning electron microscopy (FE-SEM) images are essential for a full evaluation of the crystal structure and morphology.



1. INTRODUCTION

Among important materials that have attracted considerable attention, AZrO₃ zirconate perovskites (A = Pb, Ca, Sr, and Ba) have been used in several technological applications as electronic conductors,¹ proton conductors,^{2–6} memory devices,⁷ thermal barriers,⁸ electronic devices,⁹ high-voltage applications,¹⁰ radioluminescence,¹¹ and photoluminescence.^{12,13} In particular, BaZrO₃ (BZO) is characterized by a very high structural and thermal congruent melting point of about 2600 °C, with a small thermal expansion coefficient, and low thermal conductivity, besides excellent mechanical and structural integrity under extreme thermal conditions associated with high stability under severe heating.^{14–18} These exceptional properties lead to applications in electroceramics and refractories¹⁵ and as a protective agent against corrosion of applied superconductors.¹⁴ To enhance their physical properties, the semiconductor, such as BZO, usually needs high crystallinity and various regular shapes.

Crystalline materials have a particular interest, because their symmetry provides a fundamental template upon which functional shapes can be developed. In particular, these properties have been successful in controlling the size, shape, and crystal structure (polymorph) of a wide range of materials, where the link between

form and function is most prevalent. One of the objectives of material science is to engineer individual components with atomic-level precision for use in the next generation of electronic devices.¹⁹

The ability to tailor properties to optimize performance requires a detailed understanding of the relationship between the electronic and material structures. Particularly, photoluminescence (PL) spectroscopy is one of the most powerful methods for studying the order–disorder effects in semiconductors and is a quantum phenomenon. To observe PL emissions, certain localized states should be present in the forbidden band gap. Localized states can exist in BZO crystals if a certain quantity of oxygen vacancies, impurities, and/or tilts are present in the structure.¹³

We found that a series of structurally disordered perovskites, synthesized by a soft chemical process called the polymeric precursor method, show intense PL at room temperature when excited by a 488 nm laser excitation line.^{20–24} We have reported several interesting properties of these ordered–disordered materials, including the fact that X-ray absorption near edge

Received: December 15, 2010

Revised: March 15, 2011

Published: April 12, 2011

spectroscopy (XANES) results of the SrTiO_3 disordered powders²⁴ pointed to the coexistence of two types of environments for titanium, namely, a 5-fold $[\text{TiO}_5]$ square-based pyramid and a 6-fold coordinated $[\text{TiO}_6]$ octahedron. The order was related to the presence of $[\text{TiO}_6]$ clusters, whereas the disorder was related to the presence of $[\text{TiO}_5]$ clusters. Ab initio calculations showed that localized levels above the valence band (VB) and below the conduction band (CB) appear in theoretical disordered models and a charge transfer occurs from the $[\text{TiO}_5]$ cluster to the $[\text{TiO}_6]$ one. These additional levels explain the wide PL emission observed in disordered materials.^{22,23} Furthermore, this theory was expanded to understand the role of modifier lattice,²⁵ and the interplay between the modifier and the former lattice was refined with the concept of complex clusters.^{26–28} More recently, by use of microwave-assisted hydrothermal synthesis, several highly crystalline perovskites with nanoassembled morphology were obtained.^{29,30} Rietveld results of well-ordered CaTiO_3 nanoparticles assisted by a hydrothermal microwave process points out changes in the intermediate range order between apex-to-apex $[\text{BO}_6]$ clusters which generate freezing distorted angles between the clusters and play an important role in the PL emission.²⁹ These distortions and tilts are important in the formation of hole–electron pairs and their final recombination.

Similarly, BZO crystals revealed blue-green PL emission at room temperature as a result of freezing distortions in the periodic lattice³⁰ and posed a challenge to determine remaining freezing defects. Thus, the implementation of periodic first-principles calculations based on density functional theory (DFT) is appropriate to modulate the intermediate freezing defect produced in cubic nanocrystalline BZO as well as electronic properties leading to very intense PL emission. The results of this work are discussed in terms of density of states, band structure, and charge density distributions which are compared with reported quantum mechanical calculations as well as available experimental data.

2. COMPUTING METHOD AND MODEL SYSTEM

The periodic DFT calculations with B3LYP^{31–33} were performed by using the CRYSTAL06 computer code.³⁴ This function is known to simulate the energetic, geometric, and electronic properties of materials with significant accuracy²¹ and has already been successfully employed.^{12,35} The atomic centers have been described by all-electron basis sets for Ba and Zr (available from <http://www.tcm.phy.cam.ac.uk/~mdt26/crystal.ht>) and 6-31G* for O atoms.³⁶

The barium zirconate structure crystallizes in the cubic structure, with space group $Pm\bar{3}m$.¹⁵ In this structure, the Ba is coordinated with 12 oxygen atoms in a cuboctahedral site and the Zr is coordinated with six oxygen atoms in an octahedral configuration. The experimental value of the lattice constant a is 4.192 Å.¹⁵

As a first step, an optimization of the lattice parameter a has been performed, yielding a value of 4.262 Å which is in agreement with experimental data and previous theoretical results.^{15,16,37–39} From this optimized structure, a $1 \times 1 \times 2$ supercell was constructed to represent four periodic models (see Figure 2):

- (i) The ordered BaZrO_3 structure (BZO_o) has each Zr atom surrounded by six O atoms $[\text{ZrO}_6]/[\text{ZrO}_6]$ clusters).

- (ii) The disordered BaZrO_3 structure (BZO_α) is generated by a displacement, 0.4 Å, of O6 in the $[010]$ direction. This displacement results in an angle of 158.7° for a Zr4–O6–Zr3 . This model represents two $[\text{ZrO}_6]$ distorted clusters: BZO_d and BZO_αd.
- (iii) The disordered BaZrO_3 model (BZO_d) is represented by the displacement (0.4 Å) of a Zr3 atom in the $[001]$ direction. This disorder model can be designed as a $[\text{ZrO}_6]$ perfect octahedron and a $[\text{ZrO}_5]$ square-based pyramid.
- (iv) The disordered BaZrO_3 model (BZO_αd) is a simultaneous disorder by the displacement of O6, 0.4 Å in the $[010]$ direction, and Zr3, 0.4 Å in the $[001]$ direction. This model can be interpreted as a junction of BZO_α and BZO_d models.

The BZO_d model is based on XANES resulting from the crystallization process of several ABO_3 perovskite structures which indicates the coexistence of two types of environments for the B atom. The order is related to the presence of $[\text{BO}_6]$ clusters, and the increasing disorder was related to the increasing presence of $[\text{BO}_5]$ clusters. Furthermore, the BZO_α model is based on Rietveld results of well-ordered CaTiO_3 samples obtained by the microwave-assisted hydrothermal method, which points out changes in the intermediate range order between apex-to-apex $[\text{BO}_6]$ clusters, generating freezing distorted angles between the clusters.²⁹ These types of disorder are represented by the BZO_α, BZO_d, and BZO_αd models.

It should be emphasized that the displacements which generate the theoretical models represented in this work are based on previous experimental results which occurred on the bulk, surfaces, and interfaces of our samples (to be addressed later). The theoretical simulations do not reflect the exact reality of powders but provide an interesting scheme which sheds light on the effects of structural deformation on the electronic structure.

Therefore, from a theoretical point of view and to analyze the differences in the electronic structures, it is convenient to pay attention to quantities such as band structures which can be compared to each other and independent crystal space groups. The calculated band structure also indicates the contributions of electronic states in valence and conduction bands. Band structures have been obtained at an $80\bar{k}$ point along the appropriate high-symmetry paths of the adequate Brillouin zone. Diagrams of the density of states (DOS) have been built for analysis of the corresponding electronic structures. The XcrysDen program⁴⁰ has been used to draw the band structure diagram.

3. EXPERIMENTAL SECTION

Microwave-assisted hydrothermal synthesis is a greener approach to synthesize materials in a shorter time (several minutes to hours) and with lower energy consumption (hundreds of watts). It produces efficient internal heating (in-core volumetric heating) by direct coupling of microwave energy with the molecules presents in the reaction mixture. Microwave irradiation therefore raises the temperature of the whole volume simultaneously (bulk heating), whereas in a conventionally heated vessel, the reaction mixture which is in contact with the vessel wall is heated first. Consequently, the microwave-assisted route is an important developing area of research.^{41–43}

BZO samples were synthesized as follows: 0.05 mol of $(\text{BaCl}_2 \cdot 2\text{H}_2\text{O})$ (Aldrich) and 0.05 mol of $\text{ZrOCl}_2 \cdot 8\text{H}_2\text{O}$ (Aldrich) were

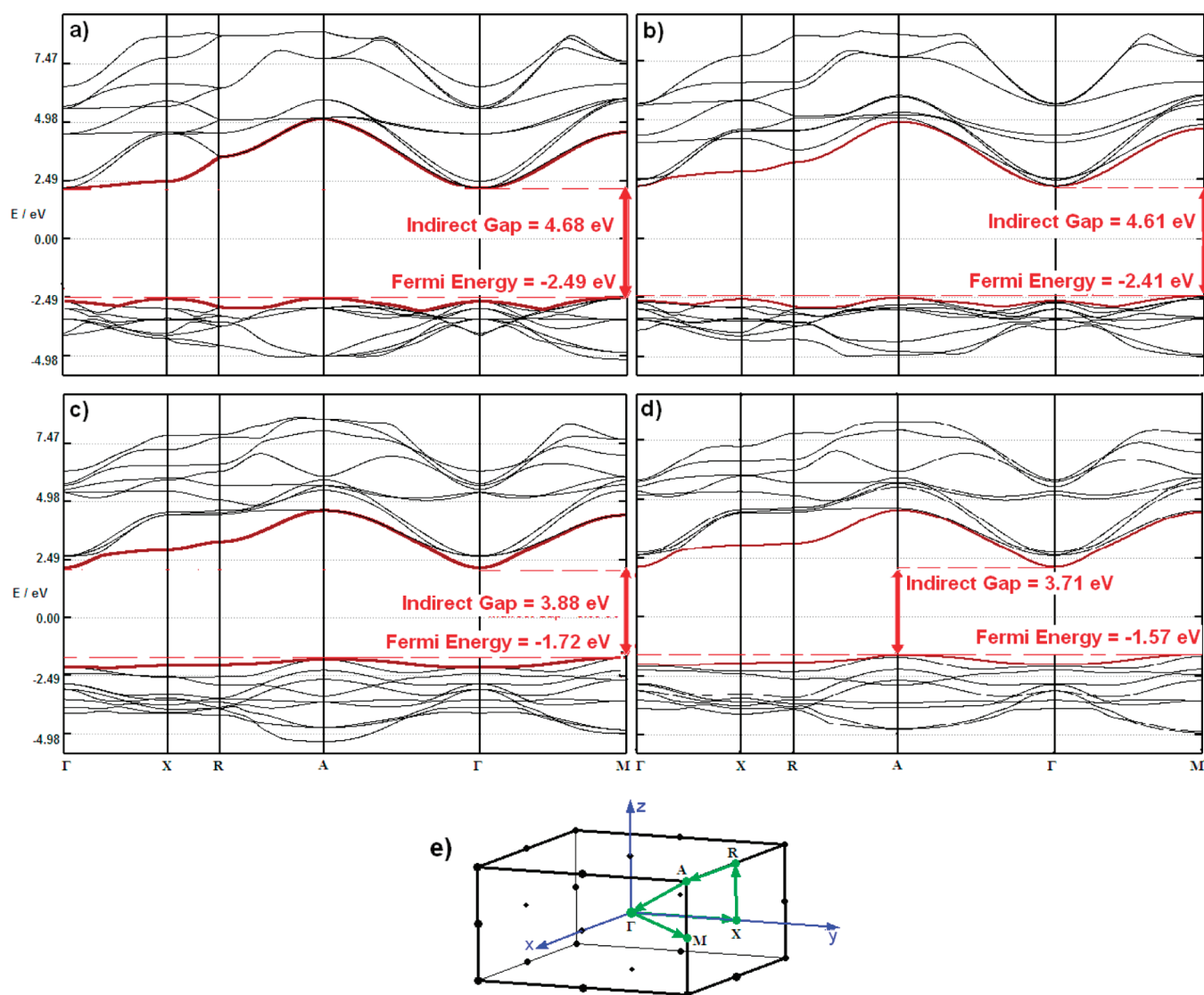


Figure 1. Band structure of BaZrO₃: (a) BZO₀; (b) BZO _{α} ; (c) BZO_d; (d) BZO _{α d}. (e) First Brillouin zone with high symmetry points for all models.

dissolved in double-distilled water and coprecipitated by 6 mol·L⁻¹ KOH (Merck) under constant stirring. The solutions were placed into a sealed polytetrafluoroethylene (PTFE) autoclave in a microwave oven (MAH) operating at 2.45 GHz on 800 W of limit power for 10 (BZO10), 20 (BZO20), 40 (BZO40), 80 (BZO80), and 160 min (BZO160) at 140 °C under a heating rate of 140 °C/min. The white powders were washed several times until a neutral pH was reached and dried for 12 h. The samples were characterized by X-ray diffraction (XRD) collected from 10° to 120° in the 2θ range using Cu K α radiation (Rigaku DMax 2500PC). Morphological characterizations were performed by field emission scanning electron microscopy (FE-SEM; Supra 35). UV–vis absorption for optical absorbance was taken using Varian Cary 5G equipment. PL spectra were collected with a Thermal Jarrel-Ash Monospec 27 monochromator and a Hamamatsu R446 photomultiplier. The 415 nm (2.98 eV) exciting wavelength of a krypton ion laser (Coherent Innova) was used with the output power of the laser kept at 200 mW. All measurements were taken at room temperature.

4. RESULTS AND DISCUSSION

Information regarding material structures at the atomic level can be considered as one of the workhorses of modern structural chemistry. This knowledge is the first step toward understanding material behavior. The difficulty of accessing such structures is an important limit to our ability to fully investigate the chemistry and physics of a system as well as hindering access to potentially useful materials.

True solid materials are incredibly complex, so it is important to emphasize that the ideal crystal formed by periodic replication of the unit cells does not exist. Real cells are exposed to lattice vibrations, contain defects, and have surface vacancies, impurities, and a nonstoichiometric composition; their presence has a significant effect on material properties.

To better describe these correlations, theoretical and experimental techniques have been implemented, obtaining essential information about structured materials and their subtle defects. Different ranges of disorder can be available at this point, allowing an overview of short-, medium-, and long-range effects.

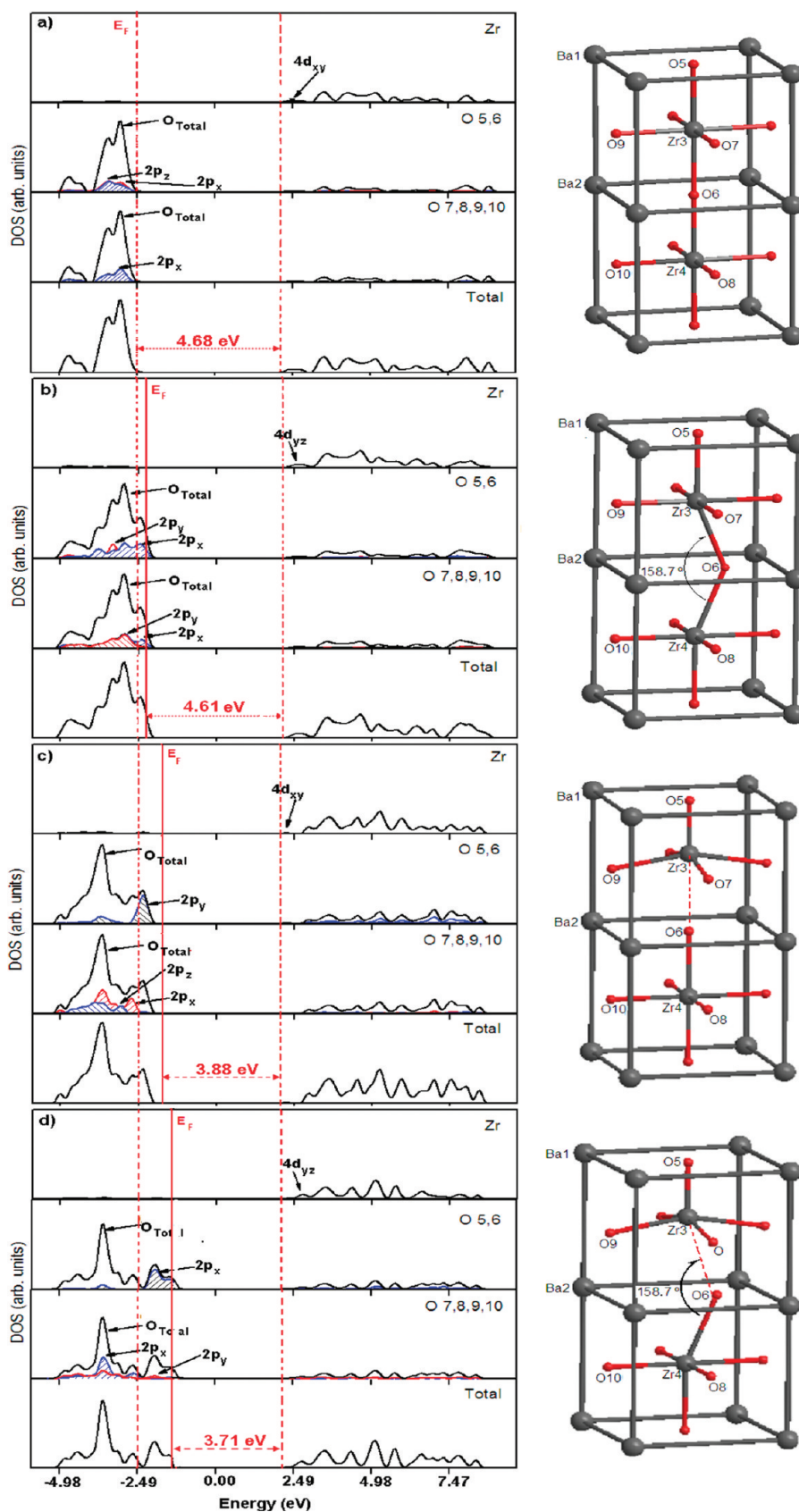


Figure 2. Total and project density of states (DOS) for (a) BZO_o, (b) BZO_α, (c) BZO_d, and (d) BZO_αd, with their specific lattice representations.

Table 1. Calculated and Experimental Optical Band Gaps (eV) and Fermi Energy (E_F) for the BZO_o, BZO_α, BZO_d, BZO_αd Models and BZO_Exp Results

	E_F	optical band gap (eV)					BZO_Exp (eV)
		Γ – Γ	X– Γ	R– Γ	A– Γ	M– Γ	
BZO_o	−2.49	4.86	4.75	5.12	4.71	4.68	BZO80: 4.99
BZO_α	−2.41	4.69	4.65	4.87	4.63	4.61	BZO40: 4.98
BZO_d	−1.72	4.29	4.21	4.18	3.96	3.88	BZO20: 4.89
BZO_αd	−1.57	4.28	4.24	3.98	3.71	3.74	BZO10: 4.78

This approach is especially useful for interpreting systems with nonequivalent units (quasi-crystals) which represent a derivation of orthodox crystallographic research.

Figure 1 shows the band structures of the BZO_o, BZO_α, BZO_d, and BZO_αd models with respective band gaps and the first Brillouin zone with symmetry points.

For the BZO_o model, the Brillouin zone top valence band (VB) is coincident with the Fermi energy, −2.49 eV (located at the Γ point). The minimum indirect band gap is 4.68 eV (located between the M and Γ points). The first conduction band (CB) between the Γ and X points is flat (see Figure 1), and an analysis of the principal atomic orbital component of selected bands indicates that the upper VB consists mainly of 2p orbitals of oxygen atoms. The bottom of the CB is composed of 4d orbitals of the Zr atoms.

For the BZO_α model, there is a displacement of the top of the VB (0.07 eV) toward the forbidden region if evaluated against the BZO_o model. This band gap is still indirect between the M and Γ points and has a value of 4.61 eV. Thus the band gap is reduced compared with the ordered system.

In the BZO_d model, the top of the VB is significantly displaced in the region of the forbidden band gap (0.77 eV) when compared to the BZO_o model. The top of the VB (−1.72 eV) is located at the Γ point, and the band gap is indirect (3.88 eV) between M and Γ . Finally, for the disordered model (BZO_αd), the band structure shows a gap of 3.71 eV. The gap remains indirect; however, the Brillouin zone was changed to between the A and Γ points in this case.

For the BZO_o model (Figure 1a), the valence bands derive from the $2p_x$, $2p_y$, and $2p_z$ orbitals of O atoms. They are separated by an indirect gap from the first conduction band which derives from the transition-metal zirconium ($4d_{xy}$, $4d_{xz}$, $4d_{yz}$) atomic orbitals designated as “ t_{2g} ” in comparison with the $[\text{ZrO}_6]$ regular cluster. Above these six bands, there are four Zr bands ($4d_{z^2-y^2}$ and $4d_{z^2}$) designated as “ e_g ”. For the displaced models (BZO_α, BZO_d, BZO_αd), although the VB is globally constituted of O ($2p_x$, $2p_y$, $2p_z$) character states, the top (the forbidden region when compared to the BZO_o model) depends mainly on the axial oxygens located at the center of the structure, O5 and O6 ($2p_x$, $2p_y$). The CB is composed of the 4d states of zirconium in an apparently random splitting of bands (Figure 1b–d).

The dislocation of the BZO_d model causes increased disorder in the lattice when compared with the BZO_α model. The greatest disorder occurs when both the angle and the distance (BZO_αd model) are displaced. This disorder is characterized by the reduction of the band gap energy in the disordered models, leading to delocalized levels and a degeneracy lift of the VB orbital and CB. Therefore, the decrease in the theoretical

band gap can be attributed to defects in the lattice, which facilitate intermediary energy levels into the band gap of disordered models.

The experimental spectral dependence of the absorbance of the samples prepared by the coprecipitation method and assisted by hydrothermal microwave annealing for 10, 20, 40, 80, and 160 min as well as the theoretical calculated band gaps are summarized in Table 1.

The optical band gap energy is related to the absorbance and photon energy by the following equation according to the Wood and Tauc method:⁴⁴ $h\nu\alpha \propto (h\nu - E_g^{\text{opt}})^2$, where α is the absorbance, h is the Planck constant, ν is the frequency, and E_g^{opt} is the optical band gap. The optical gap values for samples BZO10 and BZO20 are 4.78 and 4.89 eV, respectively, which are smaller than those for BZO40, BZO80, and BZO160 (4.99 eV). The exponential optical absorption edge and hence the optical band gap are controlled by the degree of structural order–disorder on the BZO lattice. The decrease in the band gap can be directly related to the increase in defects in the BZO lattice; in the present case, octahedral and cuboctahedral distortions raise the intermediary levels within the band gap region, reducing the optical measured band gap. Increased disorder is linked to deep defects inserted into the band gap, and increased order is also associated with shallow defects which disappear easily if total order is achieved. Thus, these results indicate that BZO10 and BZO20 are the more disordered samples. The observed optical band gap indicates only the presence of defects; hence localized electronic levels in the forbidden band gap nevertheless do not indicate specifically the structural defects that may be linked to them. Moreover, even the samples treated for prolonged periods have frozen structural defects, which are related to the use of the microwave energy acting directly on the synthesis of BZO samples.³⁰ For this propose, the theoretical models are very useful and render an interesting vision of the effect of diverse structural defects in the electronic structure and consequently in the band gap of a material.

The calculated total and atom-resolved DOS projected for models BZO_o, BZO_α, BZO_d, and BZO_αd are shown in Figure 2 and range from −5 eV below the top of the VB to 8 eV above the top of the VB band, and they represent the main orbital that influences the gap state. Analyses of the key atomic orbital (AO) of the selected bands were performed with a threshold of 0.15 au for the important eigenvector coefficients.

For BZO_o, the upper VB is composed predominantly of O(2p) states distributed in the axial O5 and O6 oxygens and the O7, O8, O9, and O10 planar oxygens of the structure (Figure 2a). For BZO_α (see Figure 2b), although the VB is also composed of O $2p_x$ and $2p_y$ states, the upper part (i.e., the new states) presents a strong axial oxygen O5 and O6 character, which are the oxygen atoms that form angles with Zr3 and Zr4. The lower CB is characterized by the $4d_{yz}$ orbital of Zr. For BZO_d (see Figure 2c), the upper part of the VB is composed mainly of the axial $2p_y$ states of oxygens O5 and O6, and the lower CB is formed by the $4d_{xy}$ orbital of Zr. The BZO_αd structure (see Figure 2d) has a strong axial $2p_x$ oxygen O5 and O6 contribution in the VB and a $4d_{yz}$ contribution of Zr in the CB. The Zr–O covalent bond creates a limited Zr(4d) contribution in the O(2p) region as well as a weak O(2p) contribution to the Zr(4d) area. On the basis of the above results, it is possible to emphasize the strong dependence among angular and bonding distortions with their respective molecular orbital redistribution.

Experimental results can now be useful to establish correlations with the simulations described above. XRD patterns of the samples treated from 10 to 160 min (corresponding to BZO10 until BZO160 samples, respectively) are presented in Figure 3, which also shows the long-range order of BZO unit cells formed by octahedrons (ZrO_6) and cuboctahedrons (BaO_{12}) more evidently after 40 min of synthesis.

Thus, only BZO40, BZO80, and BZO160 can be completely indexed as JCPDS Card No. 06-0399 with a $Pm\bar{3}m$ space group. However, the low crystallinity observed in the XRD of the BZO10 and BZO20 samples indicates that the crystallization process remains incomplete. These results agree with UV–vis measurements, indicating that BZO10 and BZO20 are more disordered structures and can be well represented by the BZO_αd model.

The size and shape of BZO crystals prepared by a hydrothermal microwave system from 10 to 160 min are evident from FE-SEM images (see Figure 4). The decaoctahedral shape is composed of 12 hexagonal faces associated with six square faces which are illustrated by inset shape simulations. This three-

dimensional architecture in fact originated from self-assembly nanoparticles as shown in Figure 4.

A relevant question to ask is what type of particles can undergo aggregation as, in principle, two scenarios can be envisaged. Most growth processes presumably start with the formation of amorphous nanoparticles which are colloidally stable as long as no precipitation is observed. Afterward as a result of a coprecipitation process, small nanocrystals are homogeneously nucleated. With decreasing colloidal stabilization (either by concentration, reaction conditions, or the consumption of stabilizer), crystal–crystal addition will occur intermediated by OH groups adsorbed on the surface. After two crystals are added, anisotropy is generated, and it is a question of interaction energy where the next particle will add. If the addition is dipole controlled, the next particle will be certainly add along the axis of the particle under isotropic growth;⁴⁵ by contrast, several shapes can originate by the assembly process.

In many cases, assembly can follow a sequence and a hierarchy of assembly steps as the first assembly structure (which did not exist before assembly) shows a more amplified tendency toward specific interactions and thus spontaneously leads to a cascade of structure formation steps. Contrary to the assembly, organization can also generate a temporal structure and order which can be destroyed and subsequently assembled in a new pathway. Admittedly, sometimes there is a diffuse borderline between mere aggregation and self-assembly. An accepted way to differentiate aggregation from assembly is the principle of cooperativity.⁴⁵

The typical morphology of particle FE-SEM images indicates a high level of defects that derive typically from the method of synthesis. As discussed previously, the theoretical models are a representation of basically two kinds of structural defects: one defect derived from a broken bond and other defect derived from a distorted bond. These defects produce an imbalanced density of charges in the network. To address this question, the choice of a Mulliken partition seems to be arbitrary, since there is no unique method of performing the charge density partition. However, the choice of a given scheme is still extremely useful in comparing the tendencies in the results of calculations performed using similar methods. The effective charges for Ba,

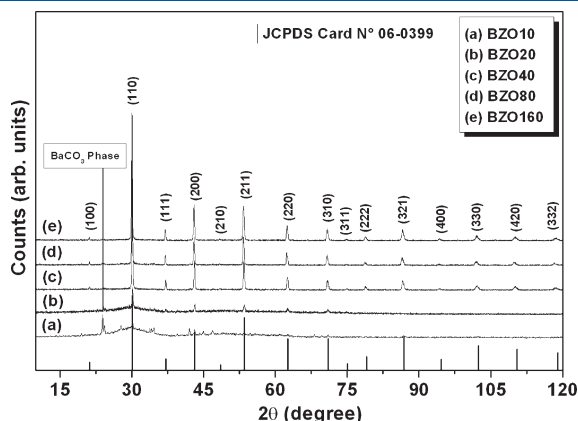


Figure 3. X-ray diffraction patterns of BZO crystals obtained by coprecipitation method and treated at hydrothermal microwave system for 10–160 min at 140 °C.

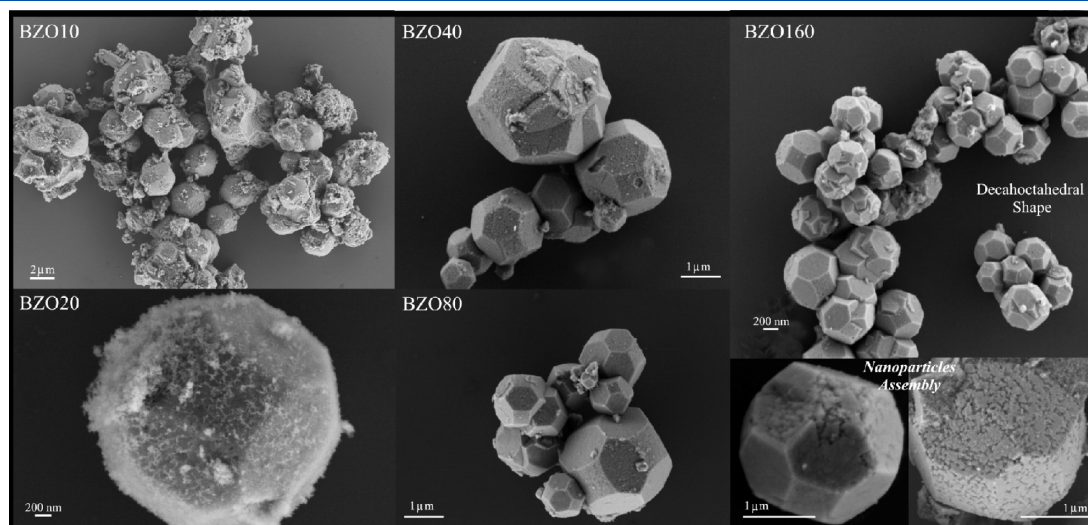


Figure 4. Typical FE-SEM images of BZO10, BZO20, BZO40, BZO80, and BZO160 decaoctahedral BZO nanoparticles toward formation of assembly.

Zr, and O present (see Table 2) are much smaller than the formal ionic charges ($4 |e|$, $2 |e|$, and $-2 |e|$, respectively).

There is no significant difference if the individual atomic charges among all models are compared. On the other hand, if the cluster charges are compared (i.e., $[\text{ZrO}_6]$, $[\text{ZrO}_5]$, $[\text{BaO}_{12}]$, and $[\text{Ba}_2\text{O}_{12}]$) suitable differences emerges.

These differences can be detected in the disordered models, but in different ways. In the BZO_α model, there is a charge imbalance between the modifier lattice clusters. In BZO_d, the imbalance is detected in both the modifier lattice and the former lattice; for BZO_αd, the imbalance is very pronounced in the former lattice and the modifier lattice. Thus a polarization of the lattice is formed in the disordered models which produce the polarized species as electrons and holes. The interaction between the former lattice and the modifier lattice, and the kind of degree of disorder between them, determines these polarized species. In the crystalline lattice, these polarized species are not localized, which facilitates a long-range effect. If the microstructure of the crystalline lattice is oriented, this polarization is amplified. This kind of effect can be observed in the distortion of nanocrystals and self-assemblies with monocrystal patterns.

Figure 5 shows electron density maps for the BZO_o, BZO_α, BZO_d, and BZO_αd models. The chosen plane is

Table 2. Mulliken Charge Distribution ($|e|$) for the BZO_o, BZO_α, BZO_d, and BZO_αd Models

	BZO_o	BZO_α	BZO_d	BZO_αd
Ba1	1.96	1.96	1.94	1.94
Ba2	1.96	1.93	1.96	1.93
Zr3	2.99	2.99	2.87	2.86
Zr4	2.99	2.99	2.98	2.98
O5	-1.65	-1.63	-1.50	-1.50
O6	-1.65	-1.71	-1.62	-1.68
O7	-1.65	-1.62	-1.65	-1.63
O8	-1.65	-1.62	-1.66	-1.61
O9	-1.65	-1.64	-1.65	-1.65
O10	-1.65	-1.64	-1.66	-1.65
$[\text{ZrO}_6]$	-1.96	-1.94	-1.90	-1.87
$[\text{ZrO}_5]$	—	—	-1.18	-1.17
$[\text{BaO}_{12}]$	-1.34	-1.39	-1.33	-1.40
$[\text{Ba}_2\text{O}_{12}]$	-1.34	-1.42	-1.31	-1.41

a vertical plane in the $[200]$ direction containing the Zr and O atoms.

An analysis of Figure 5a clearly shows that the bonding between Ti and O has a covalent bonding nature that is visible due to hybridization between the $\text{O}(2p)$ states and the $\text{Zr}(3d)$ states.

In the BZO_α model (Figure 5b), the covalent bonding nature of $\text{Zr}-\text{O}$ decreases as a consequence of the distorted angle between $[\text{ZrO}_6-\text{ZrO}_6]$ clusters which generate distorted complex clusters $[\text{ZrO}_6]_d$. However, in this plane of analysis, the two $[\text{ZrO}_6]_d$ clusters remain symmetric. The Mulliken analysis shown in Table 2 indicates that charge density changes in the $[\text{BaO}_{12}-\text{BaO}_{12}]$ clusters.

The breaking of the $\text{Zr}-\text{O}$ bond is visible in Figure 5c. The displacement of a metallic center when switching from BZO_o to BZO_d results in the deformation of a symmetric $[\text{ZrO}_6-\text{ZrO}_6]$ structure into two fragments: $[\text{ZrO}_6]$ and $[\text{ZrO}_5 \cdot \text{V}_o^z]$ complex states, where $z = x, \bullet$, and $\bullet\bullet$, and the Kröger–Vink notation is used to designate complex clusters. The charge density is modulated by the metal dislocation value, i.e., the distance between the dislocated metal and the oxygen which loses their connection. Then the $[\text{ZrO}_5 \cdot \text{V}_o^x]$ species will be linked to the neutral or ordered complex and the $[\text{ZrO}_5 \cdot \text{V}_o^\bullet]$ and $[\text{ZrO}_5 \cdot \text{V}_o^{\bullet\bullet}]$ species will be linked to an increased dislocation of metal and a more disordered structure, respectively.

The profile contours of Figure 5d are very similar to those of Figure 5c for the BZO_αd model. However, the Mulliken charge densities for $[\text{BaO}_{12}-\text{BaO}_{12}]$ clusters in Table 2 are different. This structure is the most disordered model, and the structure asymmetry generates greater imbalanced charges.

Based on the above quantum mechanical calculation results corroborated by experimental data, the possible origin of distortion freeze in the BZO lattice is available. Hence the origin of the green PL emission of these crystalline systems (see Figure 6) is apparent.

The general aspect of the spectra is a broad band covering a large part of the visible spectra (from ~ 470 to 800 nm). A set of emission bands is distinctly recorded under 415 nm wavelength, indicating that the energy of 2.99 eV was able to excite different populations of electrons existing in the forbidden band gap of crystalline nanoparticles. As the experimental gap measured was in the range $4.78-4.99$ eV, it must have additional levels in the forbidden band gap that the UV–vis measurement was not able to detect, which are evident in the PL transition (see Table 1).

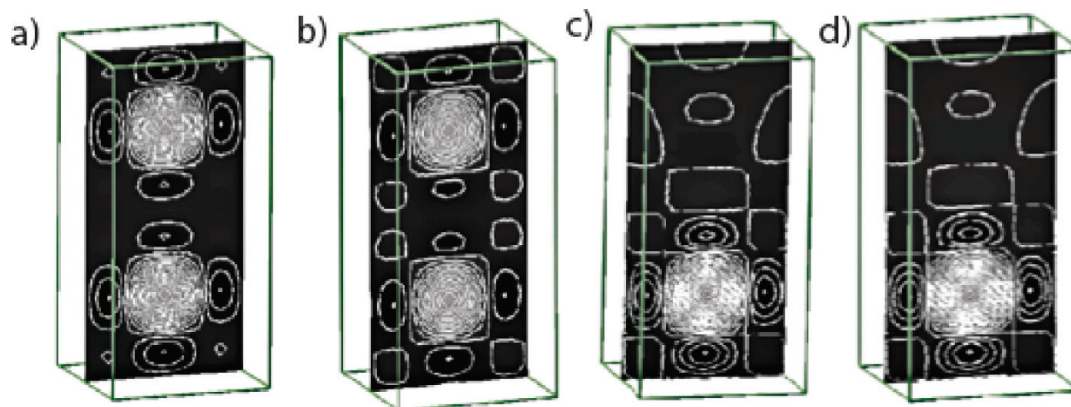


Figure 5. Electron density maps of (a) BZO_o, (b) BZO_α, (c) BZO_d, and (d) BZO_αd models.

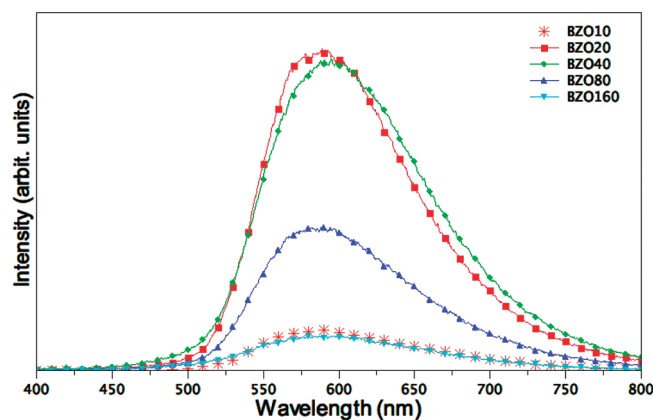


Figure 6. Photoluminescence behavior of BZO self-assembled nanocrystals in decaoctahedral shape.

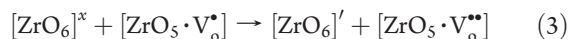
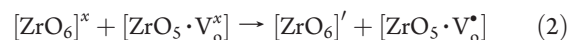
The Stokes shift can be related to the difference between the excitation and the emission maximum and represents the strength of the electron–phonon interaction. For the BZO10, BZO20, BZO80, and BZO160 samples, the Stokes shift was 169, 170, 171, and 170 nm, respectively, which was centered in the green–yellow range (around 570 nm) of the visible spectra and very close among them. The BZO40 nanoparticle has a greater Stokes shift with a maximum centered at 179 nm, indicating a dependence of electron–phonon interaction on the excitation wavelength and the degree of disorder in the lattice. This rearrangement of the lattice can be attributed to the crystallization process in the BZO10 and BZO20 nanoparticles and freezing of structural defects inside the zirconium octahedrons which is related to microwave energy acting directly on the rotational barriers of the water in the BZO40, BZO80, and BZO160 nanoparticles. Thus, the PL emission is a very sensitive measurement of structural change, and *ab initio* calculations can predict how these structural changes influence the electronic distribution and consequently the quantum properties at the molecular level of these materials.

Calculations of dislocated $[\text{ZrO}_6]$ complex clusters indicate that localized states generated in the band gap reduce the gap energies. When the structural order increases, the gap energy increases. These observations confirm the fact that PL is directly associated with the localized states existing in the band gap and that the degree of order–disorder changes these localized states.

Thus each color represents a different type of electronic transition and is linked to a specific structural arrangement or polarization of the lattice. The blue emission can be linked to shallow defects in the band gap and linked to a more ordered structure. The green, yellow, and red emissions are linked to defects deeply inserted in the band gap and to a greater disorder or polarization of the lattice.

The DOS analysis indicates that the BZO_α model is linked for a smaller decrease in the band gap than the BZO_d model. For the BZO_α model there is a tilted octahedral represented by a $[\text{ZrO}_6]_d$ complex cluster which is responsible for creating shallow defects in the band gap. The complexes $[\text{ZrO}_5 \cdot \text{V}_o^\bullet]$ and $[\text{ZrO}_5 \cdot \text{V}_o^{\bullet\bullet}]$ create deeper defects inserted in the gap. As these complexes seem to occur in the modifier lattice (i.e., in the complex formed by the $[\text{BaO}_{12}]$ clusters), the interplay between these cluster generates a specific PL intensity.

Before donor excitation, a hole in the acceptor state and an electron in the donor state are created according to the following equations:



where in our representative model we consider that $[\text{ZrO}_6]_o^x$ is the ordered cluster, $[\text{ZrO}_6]_d^x$ is the disordered or tilted cluster, $[\text{ZrO}_6]_o'$ is donor, $[\text{ZrO}_5 \cdot \text{V}_o^\bullet]$ is donors/acceptors, and $[\text{ZrO}_5 \cdot \text{V}_o^{\bullet\bullet}]$ is acceptors.

In the complex $[\text{ZrO}_6]_o'$, the clusters act as electron donors while the vacancy complex $[\text{ZrO}_5 \cdot \text{V}_o^\bullet]$ tends to trap electrons and/or holes; $[\text{ZrO}_5 \cdot \text{V}_o^{\bullet\bullet}]$ acts as an electron trap. These equations suggest that the oxygen vacancy trapped electron in the valence band is a necessary requirement for the transition of a valence band hole in the conduction band, so most electrons around oxygen vacancies are released. Therefore, such an oxygen vacancy complex site is relatively positively charged. Moreover, oxygen vacancies tend to trap photogenerated electrons. The charge transfer occurring as proposed in eqs 1 and 2 creates electrons and hole polarons that can be designated as bipolarons.

In our proposed model, the wide-band model,¹² the most important events occur before excitation, i.e., before the arrival of the photon. The short- and intermediate-range structural defects generate localized states within the band gap and a nonhomogeneous charge distribution in the cell, thereby allowing electrons to become trapped. Our model addresses the structural defects present in the crystal lattice randomly. The decrease in defect density is directly related to the increasing time of synthesis. However, the whole model is based on the crystals in their ground state (lowest energy), so a model of excited states will be welcomed in the future to clarify the electronic transitions in crystalline systems as previously described by Gracia et al.⁴⁶

The intensity of the PL emission depends mainly on the interaction of these complex clusters and the excitation wavelength. The localized levels are energetically distributed, so various energies are able to excite the trapped electrons. After the photon excitation, the recombination and decay processes follow several valid hypotheses presented in the literature.^{47,48}

Among the possible origins of structural distortions available to the BZO compound, the remaining random OH groups replacing oxygen can act as a potential factor to promote redistribution in the density of states (as discussed previously for different distortions),¹¹ which results in PL emission.

5. CONCLUSIONS

Computational studies based on first-principles simulations were important for elucidating quantum properties at the molecular level of BZO luminescent samples. Thus periodic B3LYP calculations of BZO_o, BZO_α, BZO_d, and BZO_αd models were performed based on previous experimental results to shed light on the optical behavior of decaoctahedral BaZrO_3 nanoparticles. It was found that the exponential optical absorption edge and hence the optical band gap were controlled by the degree of structural order–disorder in the BZO cubic lattice. The decrease in the band gap is directly associated with the increase in defects in the BZO lattice, which create additional levels in the

band gap. These intermediate states are surely a result of the synthesis method as well as the specific decaoctahedral morphology. Shallow defects were linked to a tilt in the octahedral $[\text{ZrO}_6]_d$ complex cluster as represented by the BZO_α model, and deep defects inserted in this region by $[\text{ZrO}_5 \cdot \text{V}_o^*]$ and $[\text{ZrO}_5 \cdot \text{V}_o^{**}]$ complexes can be related to BZO_d and BZO_αd distortions. The mismatches between these clusters create specific polarizations in the lattice and determine the profile of the PL emission band. The PL emission around 570 nm proved to be very sensitive to changes in charge density, and ab initio calculations can predict how these structural changes influence the electronic distribution. In particular, in the disordered models, the top of the VB depends on O5 and O6 atoms; i.e., these atoms are mainly responsible for new states in the forbidden region.

AUTHOR INFORMATION

Corresponding Author

*E-mail: mlucio3001@gmail.com or mlucio@liec.ufscar.br.

ACKNOWLEDGMENT

This work is supported by Brazilian Funding Agencies FAPESP, CAPES, CNPq, and INCTMN. The computer simulations were conducted in the “Laboratório de Simulação Molecular”, UNESP, Bauru, Brazil.

REFERENCES

- Kurita, N.; Xiong, Y. P.; Imai, Y.; Fukatsu, N. *Ionics* **2010**, *16*, 787.
- Gomez, M. A.; Chunduru, M.; Chigweshe, L.; Foster, L.; Fensin, S. J.; Fletcher, K. M.; Fernandez, L. E. *J. Chem. Phys.* **2010**, *132*, No. 214709.
- Bjorheim, T. S.; Kuwabara, A.; Ahmed, I.; Haugrud, R.; Stolen, S.; Norby, T. *Solid State Ionics* **2010**, *181*, 130.
- Buannic, L.; Blanc, F.; Hung, I.; Gan, Z. H.; Grey, C. P. *J. Mater. Chem.* **2010**, *20*, 6322.
- Park, J. S.; Lee, J. H.; Lee, H. W.; Kim, B. K. *Solid State Ionics* **2010**, *181*, 163.
- Omata, T.; Fuke, T.; Otsuka-Yao-Matsuo, S. *Solid State Ionics* **2008**, *179*, 1116.
- Lin, M. H.; Wu, M. C.; Lin, C. H.; Tseng, T. Y. *J. Appl. Phys.* **2010**, *107*, No. 124117.
- Ma, W.; Mack, D. E.; Vassen, R.; Stover, D. *J. Am. Ceram. Soc.* **2008**, *91*, 2630.
- Lin, C. C.; Lin, C. Y.; Lin, M. H.; Lin, C. H.; Tseng, T. Y. *IEEE Trans. Electron Devices* **2007**, *54*, 3146.
- Shende, R. V.; Krueger, D. S.; Rossetti, G. A.; Lombardo, S. J. *J. Am. Ceram. Soc.* **2001**, *84*, 1648.
- Moreira, M. L.; Volanti, D. P.; Andres, J.; Montes, P. J. R.; Valerio, M. E. G.; Varela, J. A.; Longo, E. *Scr. Mater.* **2011**, *64*, 118.
- Longo, V. M.; Cavalcante, L. S.; Erlo, R.; Mastelaro, V. R.; de Figueiredo, A. T.; Sambrano, J. R.; de Lazaro, S.; Freitas, A. Z.; Gomes, L.; Vieira, N. D.; Varela, J. A.; Longo, E. *Acta Mater.* **2008**, *56*, 2191.
- Cavalcante, L. S.; Longo, V. M.; Zampieri, M.; Espinosa, J. W. M.; Pizani, P. S.; Sambrano, J. R.; Varela, J. A.; Longo, E.; Simoes, M. L.; Paskocimas, C. A. *J. Appl. Phys.* **2008**, *103*, 063527.
- Erb, A.; Walker, E.; Flukiger, R. *Physica C* **1995**, *245*, 245.
- Yamanaka, S.; Fujikane, M.; Hamaguchi, T.; Muta, H.; Oyama, T.; Matsuda, T.; Kobayashi, S. I.; Kurosaki, K. *J. Alloys Compd.* **2003**, *359*, 109.
- Yamanaka, S.; Kurosaki, K.; Maekawa, T.; Matsuda, T.; Kobayashi, S.; Uno, M. *J. Nucl. Mater.* **2005**, *344*, 61.
- Azad, A. M.; Subramaniam, S. *Mater. Res. Bull.* **2002**, *37*, 11.
- Guillaume, B.; Boschini, F.; Garcia-Cano, I.; Rulmont, A.; Cloots, R.; Ausloos, M. *J. Eur. Ceram. Soc.* **2005**, *25*, 3593.
- Barnard, A. S. *Cryst. Growth Des.* **2009**, *9*, 4860.
- Pizani, P. S.; Basso, H. C.; Lanciotti, F.; Boschi, T. M.; Pontes, F. M.; Longo, E.; Leite, E. R. *Appl. Phys. Lett.* **2002**, *81*, 253.
- Orhan, E.; Pontes, F. M.; Pinheiro, C. D.; Boschi, T. M.; Leite, E. R.; Pizani, P. S.; Beltran, A.; Andres, J.; Varela, J. A.; Longo, E. *J. Solid State Chem.* **2004**, *177*, 3879.
- Orhan, E.; Varela, J. A.; Zenatti, A.; Gurgel, M. F. C.; Pontes, F. M.; Leite, E. R.; Longo, E.; Pizani, P. S.; Beltran, A.; Andres, J. *Phys. Rev. B* **2005**, *71*, 085113.
- Longo, E.; Orhan, E.; Pontes, F. M.; Pinheiro, C. D.; Leite, E. R.; Varela, J. A.; Pizani, P. S.; Boschi, T. M.; Lanciotti, F.; Beltran, A.; Andres, J. *Phys. Rev. B* **2004**, *69*, 125115.
- Pontes, F. M.; Longo, E.; Leite, E. R.; Lee, E. J. H.; Varela, J. A.; Pizani, P. S.; Campos, C. E. M.; Lanciotti, F.; Mastelaro, V.; Pinheiro, C. D. *Mater. Chem. Phys.* **2003**, *77*, 598.
- de Lazaro, S.; Milanez, J.; de Figueiredo, A. T.; Longo, V. M.; Mastelaro, V. R.; De Vicente, F. S.; Hernandez, A. C.; Varela, J. A.; Longo, E. *Appl. Phys. Lett.* **2007**, *90*, 111904.
- Longo, V. M.; Costa, M. D. S.; Simoes, A. Z.; Rosa, I. L. V.; Santos, C. O. P.; Andres, J.; Longo, E.; Varela, J. A. *Phys. Chem. Chem. Phys.* **2010**, *12*, 7566.
- Longo, V. M.; Cavalcante, L. S.; Costa, M. G. S.; Moreira, M. L.; de Figueiredo, A. T.; Andres, J.; Varela, J. A.; Longo, E. *Theor. Chem. Acc.* **2009**, *124*, 385.
- Moreira, M. L.; Andres, J.; Longo, V. M.; Li, M. S.; Varela, J. A.; Longo, E. *Chem. Phys. Lett.* **2009**, *473*, 293.
- Moreira, M. L.; Paris, E. C.; do Nascimento, G. S.; Longo, V. M.; Sambrano, J. R.; Mastelaro, V. R.; Bernardi, M. I. B.; Andres, J.; Varela, J. A.; Longo, E. *Acta Mater.* **2009**, *57*, 5174.
- Moreira, M. L.; Andres, J.; Varela, J. A.; Longo, E. *Cryst. Growth Des.* **2009**, *9*, 833.
- Lee, C. T.; Yang, W. T.; Parr, R. G. *Phys. Rev. B* **1988**, *37*, 785.
- Perdew, J. P.; Wang, Y. *Phys. Rev. B* **1992**, *45*, 13244.
- Becke, A. D. *J. Chem. Phys.* **1993**, *98*, 5648.
- Dovesi, R.; Saunders, V. R.; Roetti, C.; Orlando, R.; Zicovich-Wilson, C. M.; F. Pascale, B. C.; Doll, K.; Harrison, N. M.; Bush, I. J.; D'Arco, P.; Llunell, M. *CRYSTAL06*; University of Torino: Torino, Italy, 2006.
- Lazaro, S.; Longo, E.; Sambrano, J. R.; Beltran, A. *Surf. Sci.* **2004**, *552*, 149.
- Marana, N. L.; Longo, V. M.; Longo, E.; Martins, J. B. L.; Sambrano, J. R. *J. Phys. Chem. A* **2008**, *112*, 8958.
- Kingsmith, R. D.; Vanderbilt, D. *Phys. Rev. B* **1994**, *49*, 5828.
- Terki, R.; Feraoun, H.; Bertrand, G.; Aourag, H. *Phys. Status Solidi B* **2005**, *242*, 1054.
- Khenata, R.; Sahnoun, M.; Baltache, H.; Rerat, M.; Rashek, A. H.; Illes, N.; Bouhafs, B. *Solid State Commun.* **2005**, *136*, 120.
- Kokalj, A. *J. Mol. Graphics* **1999**, *17*, 176.
- Bilecka, I.; Niederberger, M. *Nanoscale* **2010**, *2*, 1358.
- Volanti, D. P.; Orlandi, M. O.; Andres, J.; Longo, E. *CrystEngComm* **2010**, *12*, 1696.
- Sczancoski, J. C.; Bomio, M. D. R.; Cavalcante, L. S.; Joya, M. R.; Pizani, P. S.; Varela, J. A.; Longo, E.; Li, M. S.; Andres, J. A. *J. Phys. Chem. C* **2009**, *113*, 5812.
- Wood, D. L.; Tauc, J. *Phys. Rev. B* **1972**, *5*, 3144.
- Colfen, H.; Antonietti, M. *Mesocrystals and Nonclassical Crystallization*; John Wiley & Sons: Chichester, England, 2008.
- Gracia, L.; Andres, J.; Longo, V. M.; Varela, J. A.; Longo, E. *Chem. Phys. Lett.* **2010**, *493*, 141.
- Leonelli, R.; Brebner, J. L. *Phys. Rev. B* **1986**, *33*, 8649.
- Eglitis, R. I.; Kotomin, E. A.; Borstel, G. *Eur. Phys. J. B* **2002**, *27*, 483.